

Making Sense of CNNs: Interpreting Deep Representations & Their Invariances with INNs

Robin Rombach*, Patrick Esser*, and Björn Ommer

Interdisciplinary Center for Scientific Computing, HCI, Heidelberg University

Abstract. To tackle increasingly complex tasks, it has become an essential ability of neural networks to learn abstract representations. These task-specific representations and, particularly, the invariances they capture turn neural networks into black box models that lack interpretability. To open such a black box, it is, therefore, crucial to uncover the different semantic concepts a model has learned as well as those that it has learned to be invariant to. We present an approach based on INNs that (i) recovers the task-specific, learned invariances by disentangling the remaining factor of variation in the data and that (ii) invertibly transforms these recovered invariances combined with the model representation into an equally expressive one with accessible semantic concepts. As a consequence, neural network representations become understandable by providing the means to (i) expose their semantic meaning, (ii) semantically modify a representation, and (iii) visualize individual learned semantic concepts and invariances. Our invertible approach significantly extends the abilities to understand black box models by enabling post-hoc interpretations of state-of-the-art networks without compromising their performance. Our implementation is available at <https://compvis.github.io/invariances/>.

1 Introduction

Key to the wide success of deep neural networks is end-to-end learning of powerful hidden representations that aim to (i) capture all task-relevant characteristics while (ii) being invariant to all other variability in the data [32,1]. Deep learning can yield abstract representations that are perfectly adapted feature encodings for the task at hand. However, their increasing abstraction capability and performance comes at the expense of a lack in interpretability [3]: Although the network may solve a problem, it does not convey an understanding of its predictions or their causes, oftentimes leaving the impression of a black box [40]. In particular, users are missing an explanation of semantic concepts that the model has learned to *represent* and of those it has learned to *ignore*, i.e. its invariances.

Providing such explanations and an understanding of network predictions and their causes is thus crucial for transparent AI. Not only is this relevant to discover limitations and promising directions for future improvements of the

* Both authors contributed equally to this work.

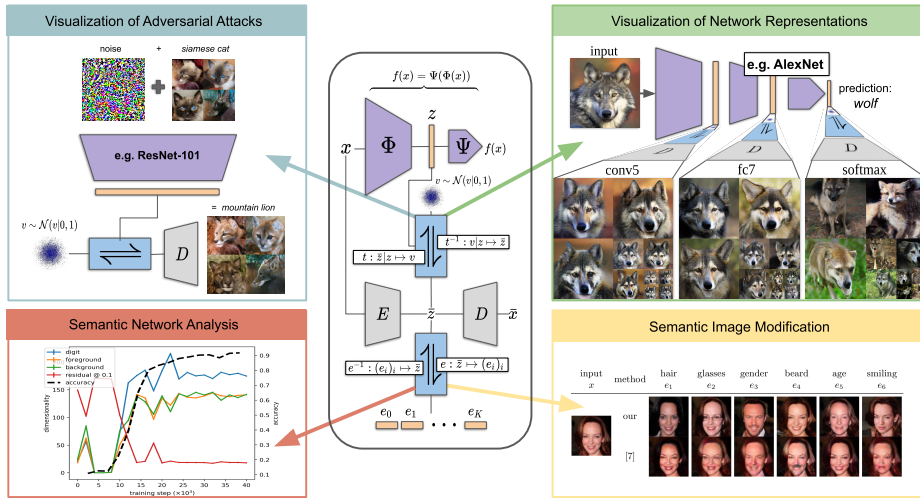


Fig. 1. Proposed architecture. We provide post-hoc interpretation for a given deep network $f = \Psi \circ \Phi$. For a deep representation $z = \Phi(x)$ a conditional INN t recovers Φ 's invariances v from a representation \tilde{z} which contains entangled information about *both* z and v . The INN e then translates the representation \tilde{z} into a factorized representation with accessible semantic concepts. This approach allows for various applications, including visualizations of network representations of natural and altered inputs, semantic network analysis and semantic image modifications.

AI system itself, but also for compliance with legislation [21,9], knowledge distillation from such a system [34], and post-hoc verification of the model [50]. Consequently, research on interpretable deep models has recently gained a lot of attention, particularly methods that investigate latent representations to understand what the model has learned [50,58,4,16,15].

Challenges & aims Assessing these latent representations is challenging due to two fundamental issues: (i) to achieve robustness and generalization despite noisy inputs and data variability, hidden layers exhibit a distributed coding of semantically meaningful concepts [17]. Attributing semantics to a single neuron via backpropagation [41] or synthesis [62] is thus impossible without altering the network [42,67], which typically degrades performance. (ii) end-to-end learning trains deep representations towards a goal task, making them invariant to features irrelevant for this goal. Understanding these characteristics that a representation has abstracted away is challenging, since we essentially need to portray features that have been discarded.

These challenges call for a method that can interpret existing network representations by recovering their invariances without modifying them. Given these recovered invariances, we seek an invertible mapping that translates a representation *and* the invariances onto understandable semantic concepts. The mapping disentangles the distributed encoding of the high-dimensional representation and its invariances by projecting them onto separate multi-dimensional factors that

correspond to human understandable semantic concepts. Both this translation and the recovering of invariances are implemented with invertible neural networks (INNs) [47,12,27]. For the translation, this guarantees that the resulting understandable representation is equally expressive as the model representation combined with the recovered invariances (no information is lost). Its invertibility also warrants that feature modifications applied in the semantic domain correctly adjust the recovered representation.

Our contributions to a comprehensive understanding of deep representations are as follows: (i) We present an approach, which, by utilizing invertible neural networks, improves the understanding of representations produced by existing network architectures with no need for re-training or otherwise compromising their performance. (ii) Our generative approach is able to recover the invariances that result from the non-injective projection (of input onto a latent representation) which deep networks typically learn. This model then provides a probabilistic visualization of the latent representation and its invariances. (iii) We bijectively translate an arbitrarily abstract representation and its invariances via a non-linear transformation into another representation of equal expressiveness, but with accessible semantic concepts. (iv) The invertibility also enables manipulation of the original latent representations in a semantically understandable manner, thus facilitating further diagnostics of a network.

2 Background

Two main approaches to interpretable AI can be identified, those which aim to incorporate interpretability directly into the design of models, and those which aim to provide interpretability to existing models [42]. Approaches from the first category range from modifications of network architectures [67], over regularization of models encouraging interpretability [38,46], towards combinations of both [64]. However, these approaches always involve a trade-off between model performance and model interpretability. Being of the latter category, our approach allows to interpret representations of existing models without compromising their performance.

To better understand what an existing model has learned, its representations must be studied [50]. [58] shows that both random directions and coordinate axes in the feature space of networks can represent semantic properties and concludes that they are not necessarily represented by individual neurons. Different works attempt to select groups of neurons which have a certain semantic meaning, such as based on scenes [66], objects [55] and object parts [56]. [4] studied the interpretability of neurons, and found that a rotation of the representation space spanned by the neurons decreases its interpretability. While this suggests that the neurons provide a more interpretable basis compared to a random basis, [16] shows that the choice of basis is not the only challenge for interpretability of representations. Their findings demonstrate that learned representations are distributed, *i.e.* a single semantic concept is encoded by an activation pattern involving multiple neurons, and a single neuron is involved in the encoding of

multiple different semantic concepts. Instead of selecting a set of neurons directly, [15] learns an INN that transforms the original representation space to an interpretable space, where a single semantic concept is represented by a known group of neurons and a single neuron is involved in the encoding of just a single semantic concept. However, to interpret not only the representation itself but also its invariances, it is insufficient to transform only the representation itself. Our approach therefore transforms the latent representation space of an auto-encoder, which has the capacity to represent its inputs faithfully, and subsequently translates a model representation and its invariances into this space for semantic interpretation and visualization.

A large body of works approach interpretability of existing networks based on visualizations. [53] uses gradients of network outputs with respect to a convolutional layer to obtain coarse localization maps. [3] proposes an approach to obtain pixel-wise relevance scores for a specific class of models which is generalized in [41]. To obtain richer visual interpretations, [63,57,62,39] reconstruct images which maximally activate certain neurons. [45] uses a generator network for this task, which was introduced in [13] for reconstructing images from their feature representation. Our key insight is that these existing approaches do not explicitly account for the invariances learned by a model. Invariances imply that feature inversion is a one-to-many mapping and thus they must be recovered to solve the task. Recently, [54] introduced a GAN-based approach that utilizes features of a pre-trained classifier as a semantic pyramid for image generation. [44] used samples from an autoregressive model of images conditioned on a feature representation to gain insights into the representation’s invariances. In contrast, our approach recovers an explicit representation of the invariances, which can be recombined with modified feature representations, and thus makes the effect of modifications to representations, *e.g.* through adversarial attacks, visible.

Other works consider visual interpretations for specialized models. [51] showed that the quality of images which maximally activate certain neurons is significantly improved when activating neurons of an adversarially robust classifier. [5] explores the relationship between neurons and the images produced by a Generative Adversarial Network. For the same class of models, [19] finds directions in their input space which represent semantic concepts corresponding to certain cognitive properties. Such semantic directions have previously also been found in classifier networks [59] but requires aligned data. All of these approaches require either special training of models, are limited to a very special class of models which already provide visualizations or depend on special assumptions on model and data. In contrast, our approach can be applied to arbitrary models without re-training or modifying them, and provides both visualizations and semantic explanations, for both the model’s representation and its learned invariances.

3 Approach

Common tasks of computer vision can be phrased as a mapping from an input image x to some output $f(x)$ such as a classification of the image, a regression

(e.g. of object locations), a (semantic) segmentation map, or a re-synthesis that yields another image. Deep learning utilizes a hierarchy of intermediate network layers that gradually transform the input into increasingly more abstract representations. Let $z = \Phi(x) \in \mathbb{R}^{N_z}$ be the representation extracted by one such layer (without loss of generality we consider z to be a N_z -dim vector, flattening it if necessary) and $f(x) = \Psi(z) = \Psi(\Phi(x))$ the mapping onto the output.

An essential characteristic of a deep feature encoding z is the increasing abstractness of higher feature encoding layers and the resulting reduction of information. To explain a latent representation, we need to recover its invariances v and make z and v interpretable by learning a bijective mapping onto understandable semantic concepts, see Fig. 1. Sec. 3.1 describes our INN t to recover an encoding v of the invariances. Due to the generative nature of t , our approach can correctly sample visualizations of the model representation and its invariances without leaving the underlying data distribution and introducing artifacts. With v then available, Sec. 3.2 presents an INN e that translates t 's encoding of z and v without losing information onto disentangled semantic concepts. Moreover, the invertibility allows modifications in the semantic domain to correctly project back onto the original representation or into image space.

3.1 Recovering the Invariances of Deep Models

Learning an Encoding to Help Recover Invariances Key to a deep representation is not only the information z captures, but also what is learned to abstract away. To learn what z misses with respect to x , we need an encoding \bar{z} , which, in contrast to z , includes these invariances. Without making prior assumptions about the deep model f , autoencoders provide a generic way to obtain such an encoding \bar{z} , since they ensure that their input x can be recovered from their learned representation \bar{z} , which hence also comprises the invariances.

Therefore, we learn an autoencoder with an encoder E that provides the data representation $\bar{z} = E(x)$ and a decoder D producing the data reconstruction $\bar{x} = D(\bar{z})$. Sec. 3.2 will utilize the decoding from \bar{z} to \bar{x} to visualize both z and v . The autoencoder is trained to reconstruct its inputs by minimizing a perceptual metric between input and reconstruction, $\|x - \bar{x}\|$, as in [13]. The details of the architecture and training procedure can be found in Sec. A.1. It is crucial that the autoencoder only needs to be trained once on the training data. Consequently, the same E can be used to interpret different representations z , e.g. different models or layers within a model, thus ensuring fair comparisons between them. Moreover, the complexity of the autoencoder can be adjusted based on the computational needs, allowing us to work with much lower dimensional encodings \bar{z} compared to reconstructing the invariances directly from the images x . This reduces the computational demands of our approach significantly.

Learning a Conditional INN that Recovers Invariances Due to the reconstruction task of the autoencoder, \bar{z} not only contains the invariances v , but also the representation z . Thus, we must disentangle [14,33,28] v and z using a mapping $t(\cdot|z) : \bar{z} \mapsto v = t(\bar{z}|z)$ which, depending on z , extracts v from \bar{z} .

Besides extracting the invariances from a given \bar{z} , t must also enable an inverse mapping from given model representations z to \bar{z} to support a further mapping onto semantic concepts (Sec. 3.2) and visualization based on $D(\bar{z})$. There are many different x with $\Phi(x) = z$, namely all those x which differ only in properties that Φ is invariant to. Thus, there are also many different \bar{z} that this mapping must recover. Consequently, the mapping from z to \bar{z} is set-valued. However, to understand f we do not want to recover all possible \bar{z} , but only those which are likely under the training distribution of the autoencoder. In particular, this excludes unnatural images such as those obtained by DeepDream [43], or adversarial attacks [58]. In conclusion, we need to sample $\bar{z} \sim p(\bar{z}|z)$.

To avoid a costly inversion process of Φ , t must be invertible (implemented as an INN) so that a change of variables

$$p(\bar{z}|z) = \frac{p(v|z)}{|\det \nabla(t^{-1})(v|z)|} \quad \text{where } v = t(\bar{z}|z) \quad (1)$$

yields $p(\bar{z}|z)$ by means of the distribution $p(v|z)$ of invariances, given a model representation z . Here, the denominator denotes the absolute value of the determinant of Jacobian $\nabla(t^{-1})$ of $v \mapsto t^{-1}(v|z) = \bar{z}$, which is efficient to compute for common invertible network architectures. Consequently, we obtain \bar{z} for given z by sampling from the invariant space v given z and then applying t^{-1} ,

$$\bar{z} \sim p(\bar{z}|z) \iff v \sim p(v|z), \bar{z} = t^{-1}(v|z). \quad (2)$$

Since v is the invariant space for z , both are complementary thus implying independence $p(v|z) = p(v)$. Because a powerful transformation t^{-1} can transform between two arbitrary densities, we can assume without loss of generality a Gaussian prior $p(v) = \mathcal{N}(v|0, \mathbb{1})$. Given this prior, our task is then to learn the transformation t that maps $\mathcal{N}(v|0, \mathbb{1})$ onto $p(\bar{z}|z)$. To this end, we maximize the log-likelihood of \bar{z} given z , which results in a per-example loss of

$$\ell(\bar{z}, z) = -\log p(\bar{z}|z) = -\log \mathcal{N}(t(\bar{z}|z)) - \log |\det \nabla t(\bar{z}|z)|. \quad (3)$$

Minimizing this loss over the training data distribution $p(x)$ gives t , a bijective mapping between \bar{z} and (z, v) ,

$$\mathcal{L}(t) = \mathbb{E}_{x \sim p(x)} [\ell(E(x), \Phi(x))] \quad (4)$$

$$= \mathbb{E}_{x \sim p(x)} \left[\frac{1}{2} \|t(E(x)|\Phi(x))\|^2 + N_{\bar{z}} \log 2\pi - \log |\det \nabla t(E(x)|\Phi(x))| \right] \quad (5)$$

Note that both E and Φ remain fixed during minimization of \mathcal{L} .

3.2 Interpreting Representations and Their Invariances

Visualizing Representations and Invariances For an image representation $z = \Phi(x)$, Eq. (2) presents an efficient approach (a single forward pass through the INN t) to sample an encoding \bar{z} , which is a combination of z with a particular realization of its invariances v . Sampling multiple realizations of \bar{z} for

a given z highlights what remains constant and what changes due to different v : information preserved in the representation z remains constant over different samples and information discarded by the model ends up in the invariances v and shows changes over different samples. Visualizing the samples $\bar{z} \sim p(\bar{z}|z)$ with $\bar{x} = D(\bar{z})$ portrays this constancy and changes due to different v . To complement this visualization, in the following, we learn a transformation of \bar{z} into a semantically meaningful representation which allows to uncover the semantics captured by z and v .

Learning an INN to Produce Semantic Interpretations The auto-encoder representation \bar{z} is an equivalent representation of (z, v) but its feature dimensions do not necessarily correspond to semantic concepts [17]. More generally, without supervision, we cannot reliably discover semantically meaningful, explanatory factors of \bar{z} [37]. In order to explain \bar{z} in terms of given semantic concepts, we apply the approach of [15] and learn a bijective transformation of \bar{z} to an interpretable representation $e(\bar{z})$ where different groups of components, called factors, correspond to semantic concepts.

To learn the transformation e , we parameterize e by an INN and assume that semantic concepts are defined implicitly by pairs of images, *i.e.* for each semantic concept we have access to training pairs x^a, x^b that have the respective concept in common. For example, the semantic concept ‘smiling’ is defined by pairs of images, where either both images show smiling persons or both images show non-smiling persons. Applying this formulation, input pairs which are similar in a certain semantic concept are similar in the corresponding factor of the interpretable representation $e(\bar{z})$.

Following [15], the loss for training the invertible network e is then given by

$$\mathcal{L}(e) = \mathbb{E}_{x^a, x^b} [-\log p(e(E(x^a)), e(E(x^b))) - \log|\det \nabla e(E(x^a))| - \log|\det \nabla e(E(x^b))|]. \quad (6)$$

Further details regarding the application of this approach within our setting can be found in the supplementary, Sec. A.2.

Interpretation by Applying the Learned INNs After training, the combination of e with t from Sec. 3.1 provides semantic interpretations given a model representation z : Eq. (2) gives realizations of the invariances v which are combined with z to produce $\bar{z} = t^{-1}(v|z)$. Then e transforms \bar{z} without loss of information into a semantically accessible representation $(e_i)_i = e(\bar{z}) = e(t^{-1}(v|z))$ consisting of different semantic factors e_i . Comparing the e_i for different model representations z and invariances v allows us to observe which semantic concepts the model representation $z = \Phi(\cdot)$ is sensitive to, and which it is invariant to.

Semantic Modifications of Latent Representations t^{-1} and e not only interpret a representation z in terms of accessible semantic concepts $(e_i)_i$. Given

Table 1. FID scores for layer visualizations of *AlexNet*, obtained with our method and [13] (D&B). Scores are calculated on the *Animals* dataset.

layer	conv5	fc6	fc7	fc8	output
ours	23.6 ± 0.5	24.3 ± 0.7	24.9 ± 0.4	26.4 ± 0.4	27.4 ± 0.3
D&B	25.2	24.9	27.2	36.1	352.6

$v \sim p(v)$, they also allow to modify $\bar{z} = t^{-1}(v|z)$ in a semantically meaningful manner by altering its corresponding $(e_i)_i$ and then applying the inverse translation e^{-1} ,

$$\bar{z} \xrightarrow{e} (e_i) \xrightarrow{\text{modification}} (e_i^*) \xrightarrow{e^{-1}} \bar{z}^* \quad (7)$$

The modified representation \bar{z}^* is then readily transformed back into image space $\bar{x}^* = D(\bar{z}^*)$. Besides visual interpretation of the modification, \bar{x}^* can be fed into the model $\Psi(\Phi(\bar{x}^*))$ to probe for sensitivity to certain semantic concepts.

4 Experiments

To explore the applicability of our approach, we conduct experiments on several models which we aim to understand: *SqueezeNet* [24], which provides lightweight classification, *FaceNet* [52], a baseline for face recognition and clustering, trained on the *VGGFace2 dataset* [7], and variants *ResNet* [22], a popular architecture, often used when finetuning a classifier on a specific task and dataset.

Experiments are conducted on the following datasets: *CelebA* [36], *Animal-Faces* [35], *Animals* (containing carnivorous animals, see Sec. B.3), *ImageNet* [11] and *ColorMNIST*, which is an augmented version of the *MNIST* dataset [31], where both background and foreground have random, independent colors.

4.1 Comparison to Existing Methods

A key insight of our work is that reconstructions from a given model’s representation $z = \Phi(x)$ are impossible if the invariances the model has learned are not considered. In Fig. 2 we compare to existing methods that either try to reconstruct the image via gradient-based optimization [39] or by training a reconstruction network directly on the representations z [13]. By conditionally sampling images $\bar{x} = D(\bar{z})$, where we obtain \bar{z} via the INN t as described in Eq. (2) based on the invariances $v \sim p(v) = \mathcal{N}(0, \mathbb{1})$, we bypass this shortcoming and obtain natural images without artifacts for any layer depth. The increased image quality is further confirmed by the FID scores reported in Tab. 1.

4.2 Understanding Models

Interpreting a Face Recognition Model *FaceNet* [52] is a widely accepted baseline in the field of face recognition. This model embeds input images of human faces into a latent space where similar images have a small L_2 -distance. We













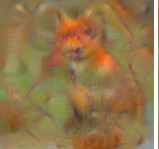
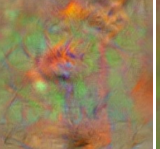
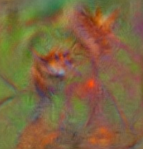
method	reconstructions \bar{x} from representations $z = \Phi(x)$ of different layers				
	input	conv5	fc6	fc7	fc8
ours					
D&B [13]					
M&V [39]					

Fig. 2. Comparison to existing network inversion methods for *AlexNet* [29]. In contrast to the methods of [13] (D&B) and [39] (M&V), our invertible method explicitly samples the invariances of Φ w.r.t. the data, which circumvents a common cause for artifacts and produces natural images independent of the depth of the layer which is reconstructed.

aim to understand the process of face recognition within this model by analyzing and visualizing learned invariances for several layers explicitly; see Tab. S12 for a detailed breakdown of the various layers of *FaceNet*. For the experiment, we use a pretrained *FaceNet* and train the generative model presented in Eq. (2) by conditioning on various layers. Fig. 3 depicts the amount of variance present in each selected layer when generating $n = 250$ samples for each of 100 different input images. This variance serves as a proxy for the amount of abstraction capability *FaceNet* has learned in its respective layers: More abstract representations allow for a rich variety of corresponding synthesized images, which results in a large variance in image space when being decoded. We observe an approximate exponential growth of learned invariances with increasing layer depth, suggesting that abstraction mainly happens in the deepest layers of the network. Furthermore, we are able to synthesize images that correspond to the given model representation for each selected layer.

How Does Relevance of Different Concepts Emerge During Training?

Humans tend to provide explanations of entities by describing them in terms of their semantics, e.g. size or color. In a similar fashion, we want to semantically understand how a network (here: *SqueezeNet*) learns to solve a given problem. Intuitively, a network should for example be able to solve a given classification problem by focusing on the relevant information while discarding task-irrelevant

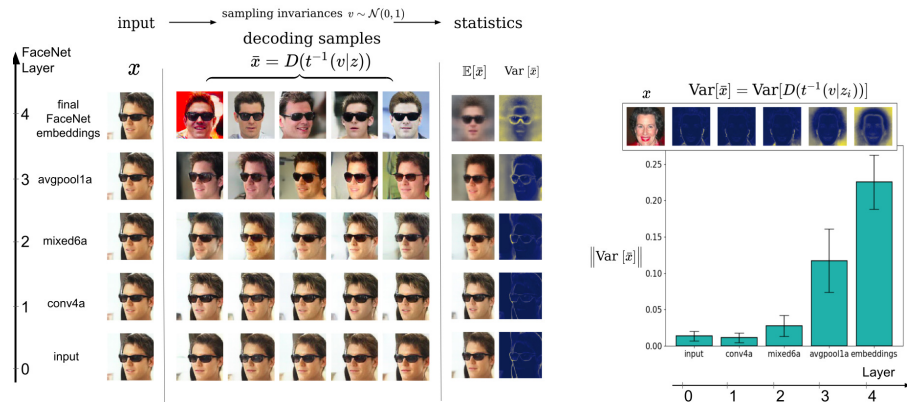


Fig. 3. *left:* Visualizing *FaceNet* representations and their invariances. Sampling multiple reconstructions $\bar{x} = D(t^{-1}(v|z))$ shows the degree of invariance learned by different layers. The invariance w.r.t. pose increases for deeper layers as expected for face identification. Surprisingly, *FaceNet* uses glasses as an identity feature throughout all its layers as evident from the spatial mean and variance plots, where the glasses are still visible. This reveals a bias and weakness of the model. *right:* Spatially averaged variances over multiple x for different layers.

information. To build on this intuition, we construct a toy problem: Digit classification on ColorMNIST. We expect the model to ignore both the random background and foreground color of the input data, as it does not help making a classification decision. Thus, we apply the invertible approach presented in Sec. 3.2 and recover three distinct factors: *digit class*, *background color* and *foreground color*. To capture the semantic changes occurring over the course of training of this classifier, we couple 20 instances of the invertible interpretation model on the last convolutional layer, each representing a checkpoint between iteration 0 and iteration 40000 (equally distributed). The result is shown in Fig. 4: We see that the *digit* factor becomes increasingly more relevant, with its relevance being strongly correlated to the accuracy of the model.

4.3 Effects of Data Shifts on Models

This section investigates the effects that altering the input data has on the model we want to understand. We examine these effects by manipulating the input data explicitly through adversarial attacks or image stylization.

How Do Adversarial Attacks Affect Network Representations? Here, we experiment with *Fast Gradient Sign* (FGSM) attacks [20], which manipulate the input image by maximizing the objective of a given classification model. To understand how such an attack modifies representations of a given model, we first compute the image’s invariances with respect to the model as $v = t(E(x)|\Phi(x))$. For an attacked image x^* , we then compute the attacked representation as $z^* =$

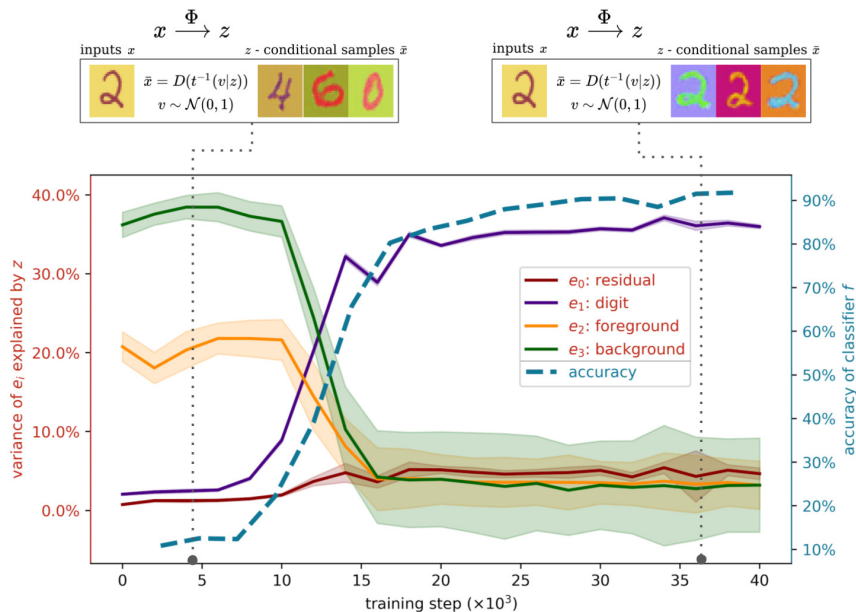


Fig. 4. Analyzing the degree to which different semantic concepts are captured by a network representation changes as training progresses. For *SqueezeNet* on *ColorMNIST* we measure how much the data varies in different semantic concepts e_i and how much of this variability is captured by z at different training iterations. Early on z is sensitive to foreground and background color, and later on it learns to focus on the digit attribute. The ability to encode this semantic concept is proportional to the classification accuracy achieved by z . At training iterations 4k and 36k we apply our method to visualize model representations and thereby illustrate how their content changes during training.

$\Phi(x^*)$. Decoding this representation with the original invariance v , allows us to precisely visualize what the adversarial attack changed. This decoding, $\bar{x}^* = D(t(v|z^*))$, is shown in Fig. 5. We observe that, over layers of the network, the adversarial attack gradually changes the representation towards its target. Its ability to do so is strongly correlated with the amount of invariances, quantified as the total variance explained by v (see Sec. B.2), for a given layer as also observed in [25]. For additional examples, see Fig. S13.

How Does Training on Different Data Affect the Model? [18] proposed the hypothesis that classification networks based on convolutional blocks mainly focus on texture patterns to obtain class probabilities. We further validate this hypothesis by training our invertible network t conditioned on pre-logits $z = \Phi(x)$ (*i.e.* the penultimate layer) of two ResNet-50 realizations. As shown in Fig. 6, a ResNet architecture trained on standard ImageNet is susceptible to the so-called "texture-bias", as samples generated conditioned on representation of pure texture images consistently show valid images of corresponding input



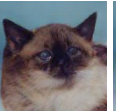
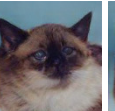



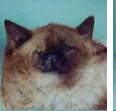
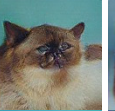
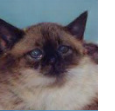


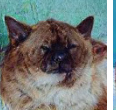
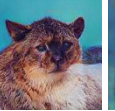
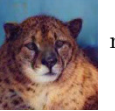
perturbation	x	visualizing perturbed representation at				prediction
		input	conv	fc	logits	
none						siamese cat
random						siamese cat
attack						mountain lion
variance of \bar{z} explained by v		11.82% (± 0.52)	7.22% (± 0.16)	49.59% (± 2.00)	84.77% (± 5.77)	

Fig. 5. Visualizing FGSM adversarial attacks on *ResNet-101*. To the human eye, the original image and its attacked version are almost indistinguishable. However, the input image is correctly classified as "siamese cat", while the attacked version is classified as "mountain lion". Our approach visualizes how the attack spreads throughout the network. Reconstructions of representations of attacked images demonstrate that the attack targets the semantic content of deep layers. The variance of \bar{z} explained by v combined with these visualizations show how increasing invariances cause vulnerability to adversarial attacks.

classes. We furthermore visualize that this behavior can indeed be removed by training the same architecture on a stylized version of ImageNet ¹; the classifier does focus on shape. Rows 10-12 of Fig. 6 show that the proposed approach can be used to generate sketch-based content with the texture-agnostic network.

4.4 Modifying Representations

Invertible access to semantic concepts enables targeted modifications of representations \bar{z} . In combination with a decoder for \bar{z} , we obtain semantic image editing capabilities. We provide an example in Fig. 7, where we modify the factors hair color, glasses, gender, beard, age and smile. We infer $\bar{z} = E(x)$ from an input image. Our semantic INN e then translates this representation into semantic factors $(e_i)_i = e(\bar{z})$, where individual semantic concepts can be modified independently via the corresponding factor e_i . In particular, we can replace each factor with that from another image, effectively transferring semantics from one representation onto another. Due to the invertibility of e , the modified representation can be translated back into the space of the autoencoder and is readily decoded to a modified image x^* . Additional examples can be found in Sec. B.5.

¹ we used weights available at <https://github.com/rgeirhos/texture-vs-shape>

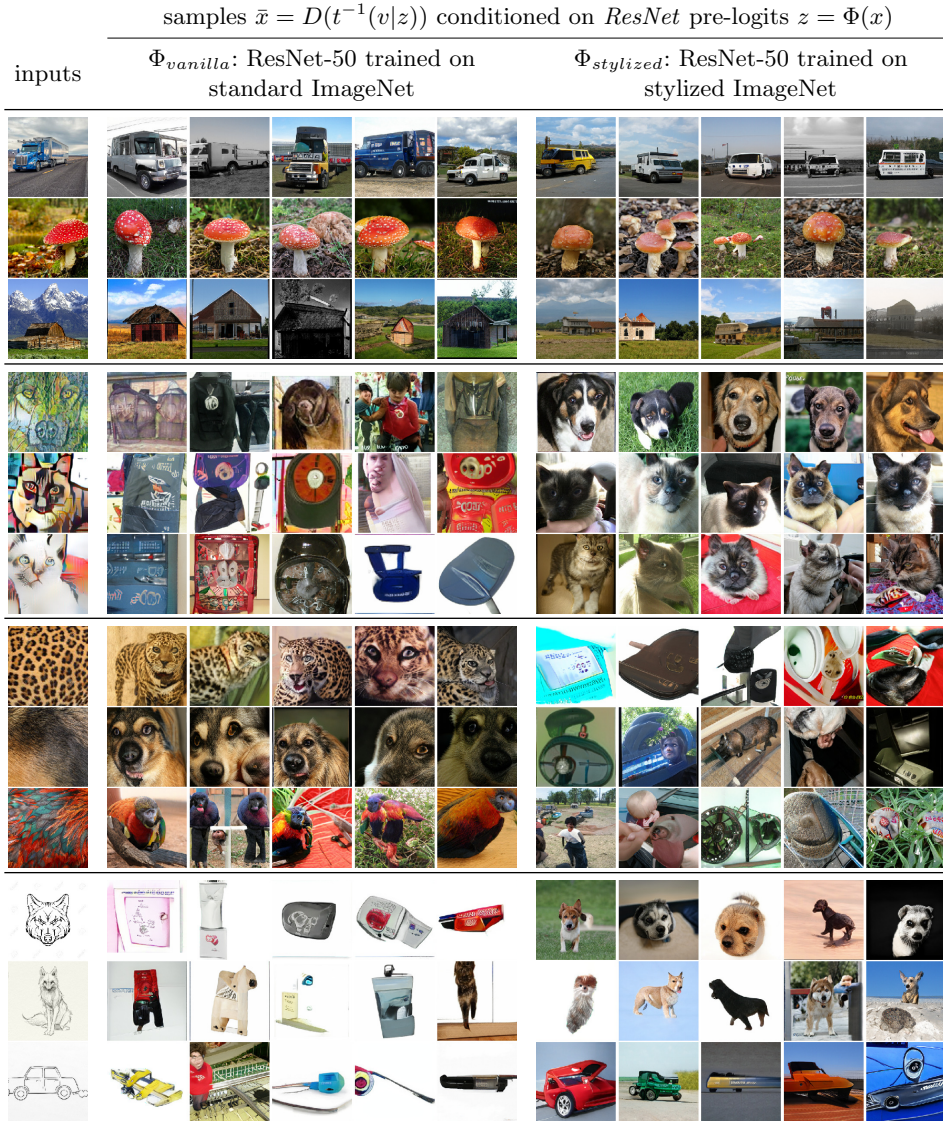


Fig. 6. Revealing texture bias in ImageNet classifiers. We compare visualizations of z from the penultimate layer of *ResNet-50* trained on standard ImageNet (left) and a stylized version of ImageNet (right). On natural images (rows 1-3) both models recognize the input, removing textures through stylization (rows 4-6) makes images unrecognizable to the standard model, however it recognizes objects from textured patches (rows 7-9). Rows 10-12 show that a model without texture bias can be used for sketch-to-image synthesis.















input x	hair e_1	glasses e_2	gender e_3	beard e_4	age e_5	smiling e_6
						
						
mean embedding	0.872	1.000	1.061	0.803	0.874	0.833
distance (\pm std)	(± 0.048)	(± 0.046)	(± 0.030)	(± 0.041)	(± 0.053)	(± 0.034)

Fig. 7. Semantic Modifications on CelebA. For each column, after inferring the semantic factors (e_i) $_i = e(E(x))$ of the input x , we replace one factor e_i by that from another randomly chosen image that differs in this concept. The inverse of e translates this semantic change back into a modified \bar{z} , which is decoded to a semantically modified image. Distances between *FaceNet* embeddings before and after modification demonstrate its sensitivity to differences in gender and glasses (see also Fig. 3).

To observe which semantic concepts *FaceNet* is sensitive to, we compute the average distance $\|f(x) - f(x^*)\|$ between its embeddings of x and semantically modified x^* over the test set (last row in Fig. 7). Evidently, *FaceNet* is particularly sensitive to differences in gender and glasses. The latter suggests a failure of *FaceNet* to identify persons correctly after they put on glasses.

5 Conclusion

Understanding a representation in terms of both its semantics and learned invariances is crucial for interpretation of deep networks. We presented an approach to (i) recover the invariances a model has learned and (ii) translate the representation and its invariances onto an equally expressive yet semantically accessible encoding. Our diagnostic method is applicable in a plug-and-play fashion on top of existing deep models with no need to alter or retrain them. Since our translation onto semantic factors is bijective, it loses no information and also allows for semantic modifications. Moreover, recovering invariances probabilistically guarantees that we can correctly visualize representations and sample them without leaving the underlying distribution, which is a common cause for artifacts. Altogether, our approach constitutes a powerful, widely applicable diagnostic pipeline for explaining deep representations.

Acknowledgments

This work has been supported in part by the German Research Foundation (DFG) projects 371923335, 421703927, and EXC 2181/1 - 390900948 and the German federal ministry BMWi within the project “KI Absicherung”.

Making Sense of CNNs: Interpreting Deep Representations & Their Invariances with INNs

Supplementary Materials

A Implementation Details

A.1 Autoencoder E, D

In Sec. 3.1, we introduced an autoencoder to obtain a representation \bar{z} of x , which includes the invariances abstracted away by a given model representation z . This autoencoder consists of an encoder $E(x)$, and a decoder $D(\bar{z})$.

Because the INNs t and e transform the distribution of \bar{z} , we must ensure a strictly positive density for \bar{z} to avoid degenerate solutions. This is readily achieved with a stochastic encoder, *i.e.* we predict mean $E(x)_\mu$ and diagonal $E(x)_{\sigma^2}$ of a Gaussian distribution, and obtain the desired representation as $\bar{z} \sim \mathcal{N}(\bar{z}|E(x)_\mu, \text{diag}(E(x)_{\sigma^2}))$.

Following [10], we train this autoencoder as a Variational Autoencoder using the reparameterization trick [26,48] to match the encoded distribution to a standard normal distribution, and jointly learn the output variance γ under an image metric $\|x - \bar{x}\|$ to avoid blurry reconstructions. The resulting loss function is thus

$$\mathcal{L}(E, D, \gamma) = \mathbb{E}_{\substack{x \sim p(x) \\ \epsilon \sim \mathcal{N}(\epsilon|0, \mathbf{1})}} \left[\frac{1}{\gamma} \|x - D(E(x)_\mu + \sqrt{\text{diag}(E(x)_{\sigma^2})} \epsilon)\| + \log \gamma \right. \\ \left. + \frac{1}{2} \sum_{i=1}^{N_{\bar{z}}} \{(E(x)_\mu)_i^2 + (E(x)_{\sigma^2})_i - 1 - \log(E(x)_{\sigma^2})_i\} \right]$$

For experiments on *ColorMNIST*, we use the squared L^2 norm for the image metric, and the encoder and decoder architectures are summarized in Tab. S1.

Table S1. Autoencoder architecture for *ColorMNIST* at resolution 28×28 .

Table S2. Encoder.	Table S3. Decoder.
RGB image $x \in \mathbb{R}^{28 \times 28 \times 3}$	$z \in \mathbb{R}^{64} \sim \mathcal{N}(\mu, \text{diag}(\sigma^2))$
Conv, Norm, LReLU $\rightarrow \mathbb{R}^{14 \times 14 \times 64}$	FC $\rightarrow \mathbb{R}^{7 \times 7 \times 128}$
Conv, Norm, LReLU $\rightarrow \mathbb{R}^{7 \times 7 \times 128}$	Conv transpose, Norm, LReLU $\rightarrow \mathbb{R}^{14 \times 14 \times 64}$
FC $\mapsto (\mu, \sigma^2) \in \mathbb{R}^{64} \times \mathbb{R}^{64}$	Conv transpose, Tanh $\rightarrow \mathbb{R}^{28 \times 28 \times 3}$

Table S4. Architectures used to compute image metrics for *CelebA*, *AnimalFaces* and *Animals* at resolution 128×128 .

Table S5. VGG-16 pretrained on ImageNet for feature extraction. Output of bold layers are used to compute feature distances.

RGB image $x \in \mathbb{R}^{128 \times 128 \times 3}$
$2 \times$ Conv, ReLU $\rightarrow \mathbb{R}^{128 \times 128 \times 64}$
MaxPool $\rightarrow \mathbb{R}^{64 \times 64 \times 64}$
$2 \times$ Conv, ReLU $\rightarrow \mathbb{R}^{64 \times 64 \times 128}$
MaxPool $\rightarrow \mathbb{R}^{32 \times 32 \times 128}$
$3 \times$ Conv, ReLU $\rightarrow \mathbb{R}^{32 \times 32 \times 256}$
MaxPool $\rightarrow \mathbb{R}^{16 \times 16 \times 256}$
$3 \times$ Conv, ReLU $\rightarrow \mathbb{R}^{16 \times 16 \times 512}$
MaxPool $\rightarrow \mathbb{R}^{8 \times 8 \times 512}$
$3 \times$ Conv, ReLU $\rightarrow \mathbb{R}^{8 \times 8 \times 512}$

Table S6. Discriminator. All convolutions use kernel size 4. Norm refers to Batch Normalization, Leaky ReLU uses slope parameter 0.2.

RGB image $x \in \mathbb{R}^{128 \times 128 \times 3}$
Conv down, LReLU $\rightarrow \mathbb{R}^{64 \times 64 \times 64}$
Conv down, Norm, LReLU $\rightarrow \mathbb{R}^{32 \times 32 \times 128}$
Conv down, Norm, LReLU $\rightarrow \mathbb{R}^{16 \times 16 \times 256}$
Conv down, Norm, LReLU $\rightarrow \mathbb{R}^{8 \times 8 \times 512}$
Conv, Norm, LReLU $\rightarrow \mathbb{R}^{8 \times 8 \times 512}$
Conv $\rightarrow \mathbb{R}^{8 \times 8 \times 1}$

For the experiments on *CelebA*, *AnimalFaces* and *Animals*, we use an improved image metric as in [13], which includes a perceptual loss and a discriminator loss. The perceptual loss consists of feature distances obtained from different layers of a fixed, pretrained network. We used a VGG-16 network pretrained on ImageNet and weighted distances of different layers as in [65]. The discriminator is trained along with the autoencoder to distinguish reconstructed images from real images using a binary classification loss, and the autoencoder maximizes the log-probability that reconstructed images are classified as real images. The architectures of VGG-16 and the discriminator are summarized in Tab. S4. For E we use an architecture based on ResNet-101 and for D we use an architecture based on BigGAN, where we include a small fully connected network to replace the class conditioning used in BigGAN by a conditioning on \bar{z} . See Tab. S7 for a summary of this autoencoder architecture.

A.2 Details on the INN for Revealing Semantics of Deep Representations

Previous works have successfully applied INNs for density estimation [12], inverse problems [2], and on top of autoencoder representations [15,61]. This section provides details on how we embed the approach of [15] to reveal the semantic concepts of autoencoder representations \bar{z} , *c.f.* Sec. 3.2.

Table S7. Autoencoder architecture for *CelebA*, *AnimalFaces* and *Animals* at resolution 128×128 .**Table S8.** *Resnet-101* based Encoder.

RGB image $x \in \mathbb{R}^{128 \times 128 \times 3}$
Conv down $\rightarrow \mathbb{R}^{64 \times 64 \times 64}$
Norm, ReLU, MaxPool $\rightarrow \mathbb{R}^{32 \times 32 \times 64}$
3× BottleNeck $\rightarrow \mathbb{R}^{32 \times 32 \times 256}$
4× BottleNeck down $\rightarrow \mathbb{R}^{16 \times 16 \times 512}$
23× BottleNeck down $\rightarrow \mathbb{R}^{8 \times 8 \times 1024}$
3× BottleNeck down $\rightarrow \mathbb{R}^{4 \times 4 \times 2048}$
AvgPool, FC $\mapsto (\mu, \sigma^2) \in \mathbb{R}^{128} \times \mathbb{R}^{128}$

Table S9. Decoder based on *BigGAN*.

$\bar{z} \in \mathbb{R}^{128} \sim \mathcal{N}(\mu, \text{diag}(\sigma^2))$
3× (FC, LReLU) $\rightarrow \mathbb{R}^{256}$
FC, Softmax $\rightarrow \mathbb{R}^{1000}$
Embed $\mapsto h \in \mathbb{R}^{128}$
FC(\bar{z}) $\rightarrow \mathbb{R}^{4 \times 4 \times 16 \cdot 96}$
ResBlock(\bar{z}, h) up $\rightarrow \mathbb{R}^{8 \times 8 \times 16 \cdot 96}$
ResBlock(\bar{z}, h) up $\rightarrow \mathbb{R}^{16 \times 16 \times 8 \cdot 96}$
ResBlock(\bar{z}, h) up $\rightarrow \mathbb{R}^{32 \times 32 \times 4 \cdot 96}$
ResBlock(\bar{z}, h) up $\rightarrow \mathbb{R}^{64 \times 64 \times 2 \cdot 96}$
Non-Local Block $\rightarrow \mathbb{R}^{64 \times 64 \times 2 \cdot 96}$
ResBlock(\bar{z}, h) up $\rightarrow \mathbb{R}^{64 \times 64 \times 96}$
Norm, ReLU, Conv up $\rightarrow \mathbb{R}^{128 \times 128 \times 3}$
Tanh $\mapsto \bar{x} \in \mathbb{R}^{128 \times 128 \times 3}$

Since we will never have examples for all relevant semantic concepts, we include a residual concept that captures the remaining variability of \bar{z} , which is not explained by the given semantic concepts.

Following [15], we learn a bijective transformation $e(\bar{z})$, which translates the non-interpretable representation \bar{z} invertibly into a factorized representation $(e_i(\bar{z}))_{i=0}^K = e(\bar{z})$, where each factor $e_i \in \mathbb{R}^{N_{e_i}}$ represents one of the given semantic concepts for $i = 1, \dots, K$, and $e_0 \in \mathbb{R}^{N_{e_0}}$ is the residual concept.

The INN e establishes a one-to-one correspondence between an encoding and different semantic concepts and, conversely, enables semantic modifications to correctly alter the original encoding (see next section). Being an INN, $e(\bar{z})$ and \bar{z} need to have the same dimensionality and we set $N_{e_0} = N_{\bar{z}} - \sum_{i=1}^K N_{e_i}$. We denote the indices of concept i with respect to $e(\bar{z})$ as $\mathcal{I}_i \subset \{1, \dots, N_{\bar{z}}\}$ such that we can write $e_i = (e(\bar{z})_k)_{k \in \mathcal{I}_i}$.

Deriving a Loss Function for Training the Semantic INN Let e_i be the factor representing some semantic concept, *e.g.* gender, that the contents of two images x^a, x^b share. Then the projection of their encodings \bar{z}^a, \bar{z}^b onto this semantic concept must be similar [15,30],

$$e_i(\bar{z}^a) \simeq e_i(\bar{z}^b) \quad \text{where } \bar{z}^a = E(x^a), \bar{z}^b = E(x^b). \quad (8)$$

Moreover, to interpret \bar{z} we are interested in the separate contribution of different semantic concepts e_i that explain \bar{z} . Hence, we seek a mapping $e(\bullet)$ that strives

to disentangle different concepts,

$$e_i(\bar{z}) \perp e_j(\bar{z}) \quad \forall i \neq j, x \quad \text{where } \bar{z} = E(x). \quad (9)$$

The objectives in Eq. (8), (9) imply a correlation in e_i for pairs \bar{z}^a and \bar{z}^b and no correlation between concepts e_i, e_j for $i \neq j$. This calls for a Gaussian distribution with a covariance matrix that reflects these requirements.

Let $e^a = (e_i^a) = (e_i(E(x^a)))$ and e^b likewise, where x^a, x^b are samples from a training distribution $p(x^a, x^b)$ for the i -th semantic concept. The distribution of pairs e^a and e^b factorizes into a conditional and a marginal,

$$p(e^a, e^b) = p(e^b|e^a)p(e^a) \quad (10)$$

Objective Eq. (9) implies a diagonal covariance for the marginal distribution $p(e^a)$, *i.e.* a standard normal distribution, and Eq. (8) entails a correlation between e_i^a and e_i^b . Therefore, the correlation matrix is $\Sigma^{ab} = \rho \text{diag}((\delta_{\mathcal{I}_i}(k))_{k=1}^{N_{\bar{z}}})$. By symmetry, $p(e^b) = p(e^a)$, which gives

$$p(e^b|e^a) = \mathcal{N}(e^b|\Sigma^{ab}e^a, \mathbf{1} - (\Sigma^{ab})^2). \quad (11)$$

Inserting Eq. (11) and a standard normal distribution for $p(e^a)$ into Eq. (10) yields the negative log-likelihood for a pair e^a, e^b . The detailed formulation can be found in the supplementary material.

Given pairs x^a, x^b as training data, another change of variables from $\bar{z}^a = E(x^a)$ to $e^a = e(\bar{z}^a)$ gives the training loss function for e as the negative log-likelihood of \bar{z}^a, \bar{z}^b ,

$$\begin{aligned} \mathcal{L}(e) = \mathbb{E}_{x^a, x^b} [& -\log p(e(E(x^a)), e(E(x^b))) \\ & -\log|\det \nabla e(E(x^a))| -\log|\det \nabla e(E(x^b))|] \end{aligned} \quad (12)$$

For simplicity we have derived the loss for a single semantic concept e_i . Simply summing over the losses of different semantic concepts yields their joint loss function and allows us to learn a joint translator e for all of them.

Log-likelihood of Pairs The loss for e in Eq. (12) contains the log-likelihood of pairs e^a, e^b . Inserting Eq. (11) and a standard normal distribution for $p(e^a)$ into Eq. (10) yields

$$-\log p(e^a, e^b) = \frac{1}{2} \left(\sum_{k \in \mathcal{I}_i} \frac{(e_k^b - \rho e_k^a)^2}{1 - \rho^2} + \sum_{k \in \mathcal{I}_i^c} (e_k^b)^2 + \sum_{k=1}^{N_{\bar{z}}} (e_k^a)^2 \right) + C \quad (13)$$

where $C = C(\rho, N_{\bar{z}})$ is a constant that can be ignored for the optimization process. $\rho \in (0, 1)$ determines the relative importance of loss terms corresponding to the similarity requirement in Eq. (8) and the independence requirement in Eq. (9). We use a fixed value of $\rho = 0.9$ for all experiments.

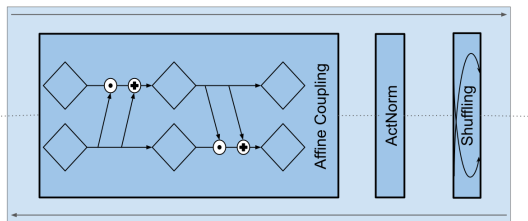


Fig. S1. A single invertible block used to build our invertible neural networks.

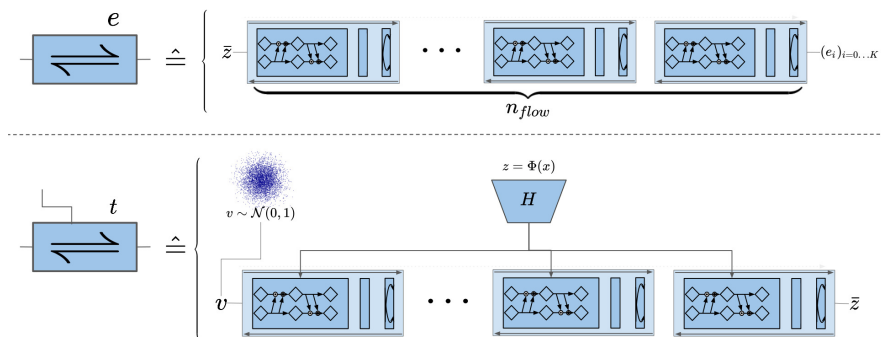


Fig. S2. Architectures of our INN models. *top:* The semantic INN e consists of stacked invertible blocks. *bottom:* The conditional INN t is composed of a embedding module H that downsamples (upsamples if necessary) a given model representation $h = H(z) = H(\Phi(x))$. Subsequently, h is concatenated to the inputs of each block of the invertible model.

Architecture of the Semantic INN In our implementation, e is built by stacking invertible blocks, see Fig. S1, which consist of three invertible layers: coupling blocks [12], actnorm layers [27] and shuffling layers. The final output is split into the factors (e_i) , see Fig. S2.

Coupling blocks split their input $x = (x_1, x_2)$ along the channel dimension and use fully connected neural networks s_i and t_i to perform the following computation:

$$\tilde{x}_1 = x_1 \cdot s_1(x_2) + t_1(x_2) \quad (14)$$

$$\tilde{x}_2 = x_2 \cdot s_2(\tilde{x}_1) + t_2(\tilde{x}_1) \quad (15)$$

Actnorm layers consist of learnable shift and scale parameters for each channel, which are initialized to ensure activations with zero mean and unit variance on the first training batch. Shuffling layers use a fixed, randomly initialized permutation to shuffle the channels of its input, which provides a better mixing of channels for subsequent coupling layers.

A.3 Conditional INN for Recovering Invariances of Deep Representations

Architecture of the Conditional INN: We build the conditional invertible neural network t by expanding the semantic model e as follows: Given a model representation z , which is used as the conditioning of the INN, we first calculate its embedding

$$h = H(z) \quad (16)$$

which is subsequently fed into the affine coupling block:

$$\tilde{x}_1 = x_1 \cdot s_1(x_2, h) + t_1(x_2, h) \quad (17)$$

$$\tilde{x}_2 = x_2 \cdot s_2(\tilde{x}_1, h) + t_2(\tilde{x}_1, h) \quad (18)$$

where s_i and t_i are modified from Eq. (15) such that they are capable of processing a concatenated input (x_i, h) . The embedding module H is usually a shallow convolutional neural network, used to down-/upsample a given model representation z to a size that the networks s_i and t_i are able to process. This means that t , analogous to e , consists of stacked invertible blocks, where each block is composed of coupling blocks, actnorm layers and shuffling layers, *c.f.* Sec. A.2 and Fig. S1. The complete architectures of both t and e are depicted in Fig. S2. Additionally, Fig. S3 provides a graphical distinction of the training and testing process of t . During training, the autoencoder $D \circ E$ provides a representation of the data that contains both the invariances and the representation of some model w.r.t. the input x . After training of t , the encoder may be discarded and visual decodings and/or semantic interpretations of a model representation z can be obtained by sampling and transforming v as described in Eq. (2).

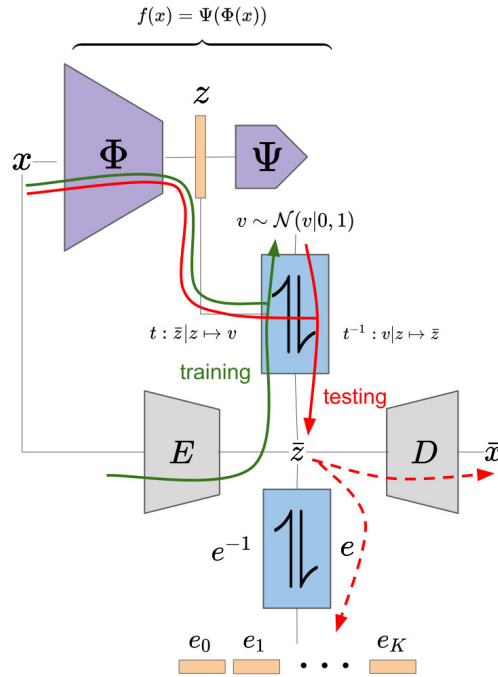


Fig. S3. Graphical distinction of information flow during training and inference. During training of t , the encoder E provides an (approximately complete) data representation, which is used to learn the invariances of a given model’s representations z . At inference, the encoder is not necessarily needed anymore: Given a representation $z = \Phi(x)$, invariances can be sampled from the prior distribution and decoded into data space through t^{-1} .

B Evaluation Details

An overview of INN hyperparameters for all experiments is provided in Tab. S10.

B.1 Architectures of Interpreted Models

Throughout our experiments, we interpret four different models: *SqueezeNet*, *AlexNet*, *ResNet* and *FaceNet*. Summaries of each of model’s architecture are provided in Tab. S11 and Tab. S14. Implementations and pretrained weights of these models are taken from:

- *SqueezeNet (1.1)* https://pytorch.org/docs/stable/_modules/torchvision/models/squeezenet
- *ResNet*: https://pytorch.org/docs/stable/_modules/torchvision/models/resnet.html
- *AlexNet*: https://pytorch.org/docs/stable/_modules/torchvision/models/alexnet.html
- *FaceNet*: <https://github.com/timesler/facenet-pytorch>

Table S10. Hyperparameters of INNs for each experiment. n_{flow} denotes the number of invertible blocks within in the model, see Fig. S1. h_w and h_d refer to the width and depth of the fully connected subnetworks s_i and t_i .

Experiment	INN input dim.	n_{flow}	h_w	h_d
Comparison Sec.4.1	t	128	20	1024 2
Understanding Models: FaceNet Sec. 4.2	t	128	20	512 2
Understanding Models: FaceNet Sec. 4.2	e	128	12	512 2
Data Effects: Adversarial Attack Sec. 4.3	t	128	20	1024 2
Data Effects: Texture Bias Sec. 4.3	t	268	20	1024 2
Data Effects: Domain Shift Sec. B.6	t	128	20	1024 2
Modifications: FaceNet & CelebA Sec. 4.4	e	128	12	512 2

B.2 Explained Variance

To quantify the amount of invariances and semantic concepts, we use the fraction of the total variance explained by invariances (Fig. 5) and the fraction of the variance of a semantic concept explained by the model representation (Fig. 4).

Using the INN t , we can consider $\bar{z} = t^{-1}(v|z)$ as a function of v and z . The total variance of \bar{z} is then obtained by sampling v , via its prior which is a standard normal distribution, and z , via $z = \Phi(x)$ with $x \sim p_{\text{valid}}(x)$ sampled from a validation set. We compare this total variance to the average variance obtained when sampling v for a given z to obtain the fraction of the total variance explained by invariances:

$$\mathbb{E}_{x' \sim p_{\text{valid}}(x')} \left[\frac{\text{Var}_{v \sim \mathcal{N}(v|0, \mathbb{1})} t^{-1}(v|\Phi(x'))}{\text{Var}_{\substack{x \sim p_{\text{valid}}(x) \\ v \sim \mathcal{N}(v|0, \mathbb{1})}} t^{-1}(v|\Phi(x))} \right] \quad (19)$$

In combination with the INN e , which transform \bar{z} to semantically meaningful factors, we can analyze the semantic content of a model representation z . To analyze how much of a semantic concept represented by factor e_i is captured by z , we use e to transform \bar{z} into e_i and measure its variance. To measure how much the semantic concept is explained by z , we simply swap the roles of z and v in Eq. (19), to obtain

$$\mathbb{E}_{v' \sim \mathcal{N}(v'|0, \mathbb{1})} \left[\frac{\text{Var}_{x \sim p_{\text{valid}}(x)} e(t^{-1}(v'|\Phi(x)))_i}{\text{Var}_{\substack{v \sim \mathcal{N}(v|0, \mathbb{1}) \\ x \sim p_{\text{valid}}(x)}} e(t^{-1}(v|\Phi(x)))_i} \right] \quad (20)$$

Fig. 5 reports Eq. (19) and its standard error when evaluated via 10k samples, and Fig. 4 reports Eq. (20) and its standard error when evaluated via 10k samples.

Table S11. High-level architectures of FaceNet and ResNet, depicted as `pytorch`-modules. Layers investigated in our experiments are marked in bold. Spatial sizes are provided as a visual aid and vary from model to model in our experiments. If not stated otherwise, we always extract from the *last* layer in a series of blocks (*e.g.* in Tab. S13: $23 \times$ **BottleNeck down** $\rightarrow \mathbb{R}^{8 \times 8 \times 1024}$ refers to the last module in the series of 23 blocks.)

Table S12. *FaceNet*: Implementations of layers **Mixed**, **Block35**, **Block17**, **Block8** can be found at <https://github.com/timesler/facenet-pytorch>. In l.4, the representation from the **2nd** convolutional layer is extracted. Furthermore, **BN** refers to batch normalization.

RGB image $x \in \mathbb{R}^{128 \times 128 \times 3}$
$3 \times$ Conv, BN, ReLU $\rightarrow \mathbb{R}^{61 \times 61 \times 64}$
MaxPool $\rightarrow \mathbb{R}^{30 \times 30 \times 64}$
$3 \times$ Conv , BN, ReLU $\rightarrow \mathbb{R}^{13 \times 13 \times 256}$
$5 \times$ Block35 $\rightarrow \mathbb{R}^{13 \times 13 \times 256}$
Mixed down $\rightarrow \mathbb{R}^{6 \times 6 \times 896}$
$10 \times$ Block17 $\rightarrow \mathbb{R}^{6 \times 6 \times 896}$
Mixed down $\rightarrow \mathbb{R}^{2 \times 2 \times 1792}$
$5 \times$ Block8 $\rightarrow \mathbb{R}^{2 \times 2 \times 1792}$
AdaAvgPool $\rightarrow \mathbb{R}^{1 \times 1 \times 1792}$
Dropout, Linear, BN $\rightarrow \mathbb{R}^{512}$
identity embedding $\rightarrow \mathbb{R}^{512}$

Table S13. *ResNet-101*: See <https://pytorch.org/docs/stable/torchvision/models.html> for details on other variants of ResNet.

RGB image $x \in \mathbb{R}^{128 \times 128 \times 3}$
Conv down $\rightarrow \mathbb{R}^{64 \times 64 \times 64}$
Norm, ReLU, MaxPool $\rightarrow \mathbb{R}^{32 \times 32 \times 64}$
$3 \times$ BottleNeck $\rightarrow \mathbb{R}^{32 \times 32 \times 256}$
$4 \times$ BottleNeck down $\rightarrow \mathbb{R}^{16 \times 16 \times 512}$
$23 \times$ BottleNeck down $\rightarrow \mathbb{R}^{8 \times 8 \times 1024}$
$3 \times$ BottleNeck down $\rightarrow \mathbb{R}^{4 \times 4 \times 2048}$
AvgPool , FC
output $\rightarrow \mathbb{R}^{1000}$

B.3 Comparison to Existing Visualization Methods

In Sec. 4.1, we compare to existing layer inversion methods that aim to reconstruct an input x from its representation $z = \Phi(x)$. Both our method and D&B’s [13] method were trained on the *Animals* dataset, which consists of a mixture of all carnivorous mammal animal classes from *ImageNet* and all animals from the *Animals with Attributes 2* [60] dataset. Hyperparameters of our autoencoder model can be found in Tab. S7. The decoder in [13] was re-implemented based on our decoder shown in Tab. S9, where we set the latent dimension to 4096 to avoid introduction of an artificial bottleneck and allow for a fair comparison. Both methods were trained by minimizing the image metric described in Sec.A.1 and Tab. S4, where no Kullback-Leibler divergence term was used for

Table S14. High-level architectures of SqueezeNet and AlexNet, depicted as `pytorch`-modules. *C.f.* Tab.S11 for further details.**Table S15.** *SqueezeNet*. We extract the penultimate *Fire* block for interpretation in Sec. 4.2.

RGB image $x \in \mathbb{R}^{128 \times 128 \times 3}$
Conv, ReLU, MaxPool $\rightarrow \mathbb{R}^{31 \times 31 \times 64}$
$2 \times$ Fire $\rightarrow \mathbb{R}^{31 \times 31 \times 128}$
MaxPool $\rightarrow \mathbb{R}^{15 \times 15 \times 128}$
$2 \times$ Fire $\rightarrow \mathbb{R}^{15 \times 15 \times 256}$
MaxPool $\rightarrow \mathbb{R}^{7 \times 7 \times 256}$
$4 \times$ Fire $\rightarrow \mathbb{R}^{7 \times 7 \times 512}$
Dropout, Conv, ReLU $\rightarrow \mathbb{R}^{7 \times 7 \times 1000}$
AdaAvgPool $\rightarrow \mathbb{R}^{7 \times 7 \times 1000}$
output $\rightarrow \mathbb{R}^{1000}$

Table S16. *AlexNet*: The first convolution uses kernel size 11.

RGB image $x \in \mathbb{R}^{128 \times 128 \times 3}$
Conv, ReLU, MaxPool $\rightarrow \mathbb{R}^{15 \times 15 \times 64}$
Conv, ReLU, MaxPool $\rightarrow \mathbb{R}^{7 \times 7 \times 192}$
Conv, ReLU $\rightarrow \mathbb{R}^{7 \times 7 \times 384}$
$2 \times$ Conv , ReLU $\rightarrow \mathbb{R}^{7 \times 7 \times 256}$
MaxPool $\rightarrow \mathbb{R}^{3 \times 3 \times 256}$
AdaAvgPool, Flatten $\rightarrow \mathbb{R}^{9216}$
Dropout, Linear , ReLU $\rightarrow \mathbb{R}^{4096}$
Dropout, Linear , ReLU $\rightarrow \mathbb{R}^{4096}$
Linear $\rightarrow \mathbb{R}^{1000}$

D&B’s method. Images from [39] are taken from their publication. Additional visual comparisons can be found in Fig. S4, S5, S6.



Fig. S4. Additional examples for layerwise reconstructions from model representations $z = \Phi(x)$ with our method and [13] (D&B). We show 10 samples per layer representation obtained with our generative approach. Here, σ denotes the softmax function, *i.e.* reconstructions are obtained from class probabilities provided by the model. We provide a comparison of equally sized images in Fig. S6 and Fig. S5.

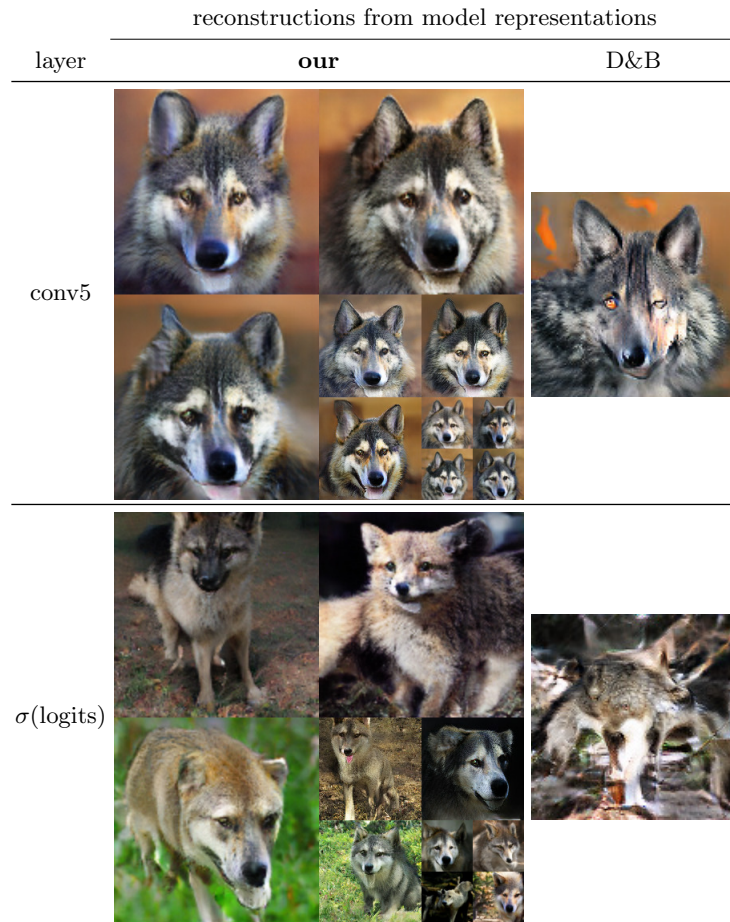


Fig. S5. Zooming into representation conditional samples for example *wolf*. To verify that our samples are outperforming those of [13] in visual quality, we repeat row 2 (conv5) and row 6 ($\sigma(\text{logits})$) of Fig. S4 with scaled images. Here, σ denotes the softmax function.

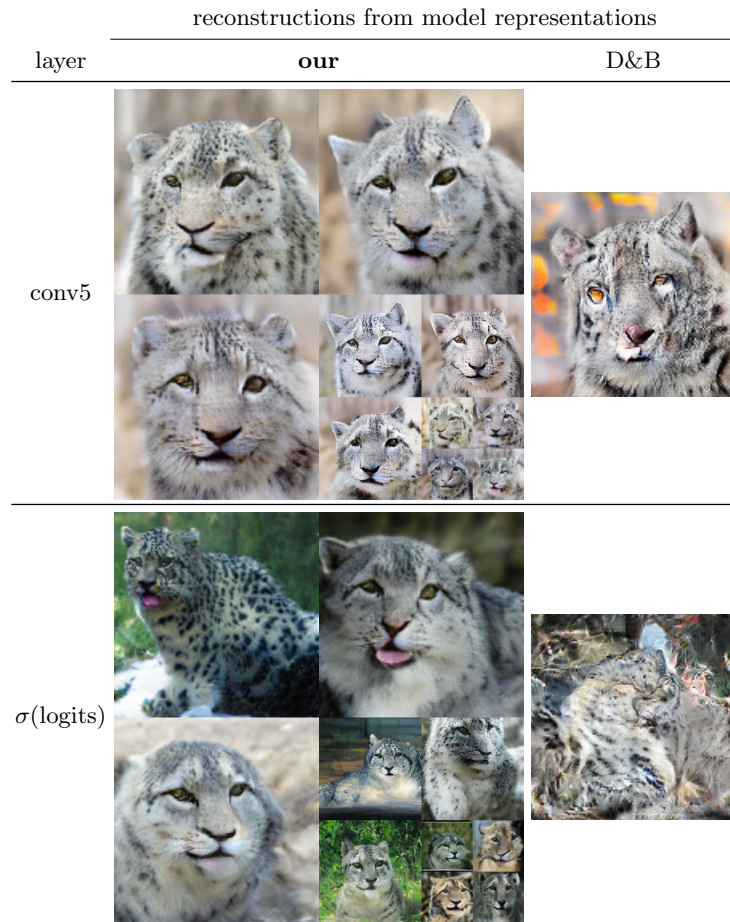


Fig. S6. Zooming into representation conditional samples for example *snow leopard*. To verify that our samples are outperforming those of [13] in visual quality, we repeat row 2 (conv5) and row 6 ($\sigma(\text{logits})$) of Fig. S4 with scaled images. Here, σ denotes the softmax function.

B.4 Relevance of Factors

input		Decoded samples $\bar{x} = D(t^{-1}(v z))$									
x		4000 training iterations					36000 training iterations				
1		6	3	7	6	4	1	1	1	1	1
4		6	3	3	5	6	4	4	4	4	4
0		9	2	4	0	9	0	0	0	0	0
8		0	3	7	6	7	8	8	8	8	8
2		6	3	3	6	4	2	2	2	2	2
7		9	2	4	0	9	7	7	7	7	7
6		0	2	8	0	8	6	6	6	6	6
8		2	2	8	8	8	8	8	8	8	8
3		9	2	4	0	8	3	3	3	3	3

Fig. S7. Additional z conditional samples after 4k and 36k training steps, as in Fig. 4. Each row is conditioned on $z = \Phi(x)$ and each column is conditioned on a $v \sim \mathcal{N}(v|0, \mathbb{1})$. At 4k (resp. 36k) iterations, z explains 2.57% (resp. 36.08%) of the variance in the digit factor. Thus, the digit class of samples obtained at 4k iterations change with the sampled invariances across columns, while it stays the same at 36k iterations. Conversely, at 4k (resp. 36k) iterations, z explains 38.44% (resp. 2.76%) of the variance in the background color factor. Thus, the background color of samples obtained at 4k iterations change with the sampled representation $z = \Phi(x)$ across rows, while it stays the same at 36k iterations.

In Sec. 4.2, we trained *SqueezeNet* for digit classification on *ColorMNIST*, which consists of *MNIST* images with randomly chosen fore- and background colors. In addition, we trained the autoencoder of Tab. S1 on *ColorMNIST* and the INN e to obtain the following factors

- e_1 representing the digit class defined by pairs of images showing the same digit in different styles and colors,
- e_2 representing the foreground color defined by pairs of images showing the same foreground color on different digits and backgrounds,
- e_3 representing the background color defined by pairs of images showing the same background color for differently colored digits.

Finally, we trained the INN t for 20 different checkpoints of *SqueezeNet* obtained between training steps zero and 40k, to obtain the stochastic mapping

from z , the penultimate *Fire* layer of *SqueezeNet*, to the semantic factors (e_i) . Fig. 4 plots Eq. (20) against the training step, with shaded areas representing the standard error obtained with 10k samples.

At step zero, *i.e.* for a randomly initialized *SqueezeNet*, we observe that the representation z mostly contains the background color and, to a lesser degree, the foreground color. This observation is consistent with the fact that color information is directly encoded in the pixel representation of the image and that there are more background pixels than foreground pixels. In contrast, information about the digit class is not directly encoded in pixel values and requires learning. As the network starts to learn between steps 10k and 15k, we indeed observe a drastic change in the semantic content of z , which becomes invariant to color information and sensitive to digit class information. Note that the network could also learn to retain color information while separating digit classes in the last classification layer, but our results demonstrate that the network learns to abstract away task-irrelevant information before that.

We show additional z conditional samples, both before and after learning, in Fig. S7.

B.5 Modifying Representations

Training Details: In Sec. 4.4 we trained the autoencoder of Tab. S7 on *CelebA* at resolution 128×128 . Using the attribute labels provided for this dataset, we trained an INN e for the semantic factors

- e_1 representing hair color, defined by pairs with the same *Black_Hair* attribute.
- e_2 representing glasses, defined by pairs with the same *Eyeglasses* attribute.
- e_3 representing gender, defined by pairs with the same *Male* attribute.
- e_4 representing beard, defined by pairs with the same *No_Beard* attribute.
- e_5 representing age, defined by pairs with the same *Young* attribute.
- e_6 representing smiling, defined by pairs with the same *Smiling* attribute.

Additional Results and Comparisons We provide a larger version of Fig. 7 with more examples in Fig. S8 and Fig. S9. While our approach aims to provide semantic understanding of representations learned by models, the invertibility of e together with the decoder D enables semantic image editing. To evaluate our approach on this task, we compare it to *StarGAN*² [8], a specialized approach for attribute modifications of face images. Our approach consistently outperforms [8] across all semantic attributes in terms of the quality of modified images, which is quantified by FID scores [23] in Fig. S9. Moreover, we observe some particular qualitative differences between our method and [8]: Changing factors with our approach produces more coherent changes, *i.e.* changes in gender cause changes in hair length (for all examples in Fig. S8), changes to an older age cause thin, white hairs (*e.g.* examples 1, 2, 6 in Fig. S8), and changes in the beard factor have no effect on female faces (*e.g.* examples 2, 3, 5, 6 in Fig. S8), suggesting that our model has learned the correct causal structure (as present in the data) where beard is caused by gender and not the other way around. In contrast, [8] produces very localized, pixelwise changes without taking the global structure into account. While such a behavior might be desired for some specialized applications, it generally leads to unnatural results, *e.g.* when changing gender, beard and age in example 2 or gender and beard in example 3 of Fig. S8.

² We used the author’s official implementation available at <https://github.com/yunjey/stargan>

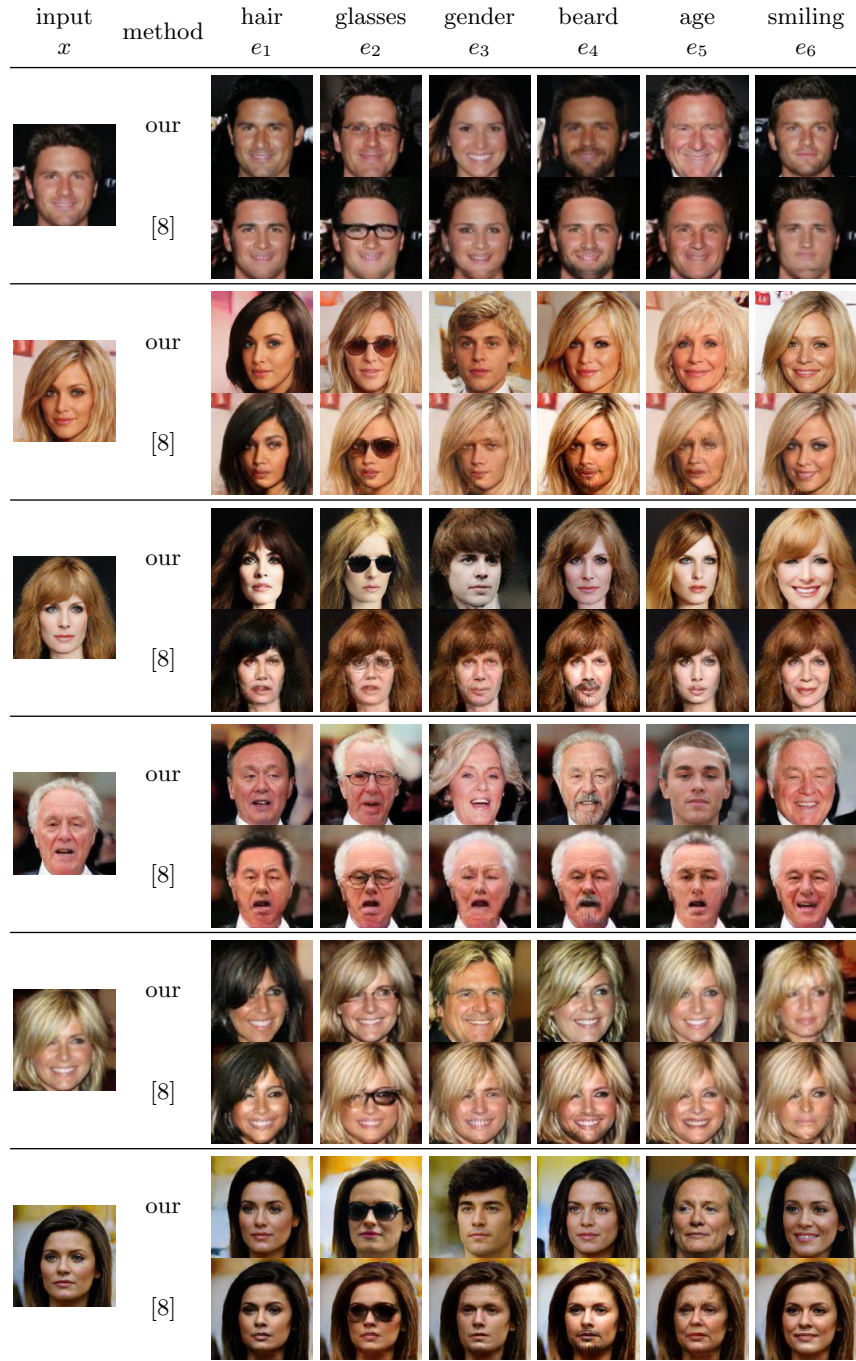


Fig. S8. Additional examples corresponding to Fig. 7. In each column, we replace a semantic factor $e_i(E(x))$ by e_i^* , which is obtained from another, randomly chosen, image that differs in the corresponding attribute (see Sec. B.5). Subsequently we decode a semantically modified image using the invertibility of e to obtain $\bar{x}^* = D(e^{-1}((e_i^*)))$. The results of *StarGAN* [8] are obtained by negating the binary value for the column's attribute. FID scores in Fig. S9.

input x	method	hair e_1	glasses e_2	gender e_3	beard e_4	age e_5	smiling e_6
	our						
	[8]						
	our						
	[8]						
	our						
	[8]						
	our						
	[8]						
	our						
	[8]						
FID	our	16.24	24.97	15.17	12.84	13.21	12.96
	[8]	20.94	41.27	20.04	19.88	21.77	14.47

Fig. S9. Additional examples as in Fig. S8. Moreover, the last row contains FID scores [23] of semantically modified images obtained by our approach and [8], which shows that our approach consistently outperforms [8].

B.6 Effects of Data Shifts - Additional Results

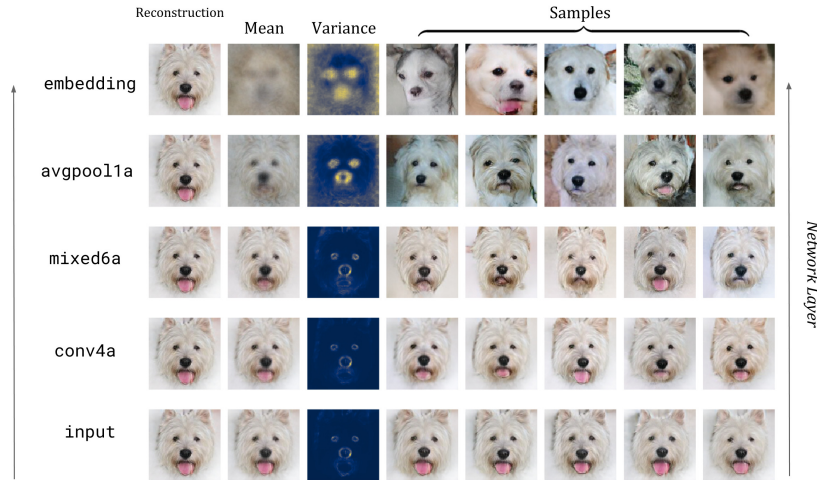


Fig. S10. Shifting domains: Human faces to animal faces evaluated with a fixed *FaceNet*. The evaluation procedure is similar to the method described in Fig. 3. Although never trained on data consisting of something else than human faces, *FaceNet* is able to capture the "identity" of the input to a certain degree. Information about appearance is approximately preserved until the last layer, *i.e.* the final identity embedding.

Data Shift from Humans to Animals As an extension of Sec. 4.3, we run an experiment on *FaceNet* and condition the invariance recovering model t on five different representations of the model (see Tab. S12) by training t on *AnimalFaces* instead of *CelebA* and an autoencoder which is trained on both *AnimalFaces* and *CelebA*, *c.f.* Tab. S7 for details. Furthermore, note that *FaceNet* is not re-trained on the new data and fixed during training, *c.f.* Fig. S3.

Fig. S10 depicts the visualized representations and corresponding learned invariances across several layers of *FaceNet*. Evidently, even deep representations of the off-domain input image may be visualized, at least as deep as the penultimate layer (**AdaAvgPool**). Another interesting result is that *FaceNet* seems to conserve class identity of the input to some degree: The appearance of samples generated by conditioning on model representations is similar, to some extent even for the last layer (**identity embedding**). This suggests that the model is able to generalize to a surprisingly large margin of data, given the input images show some kind of symmetry and perceptual similarity to human faces.

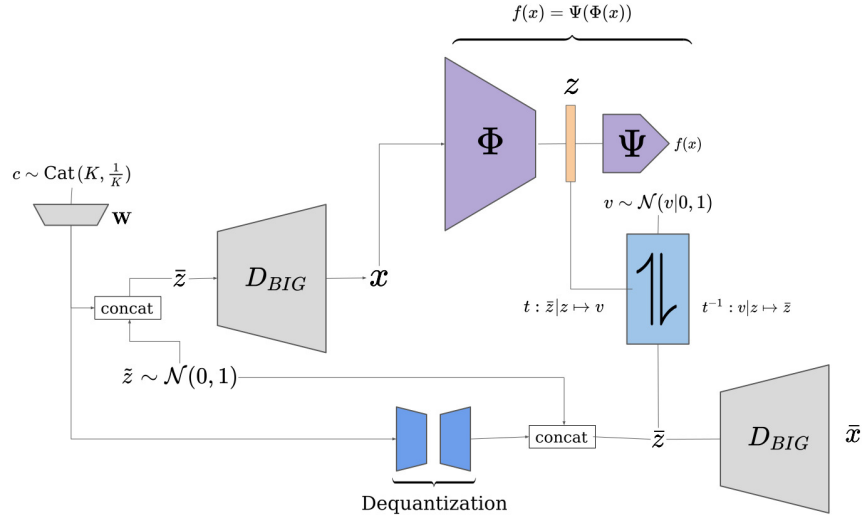


Fig. S11. Applying our approach to *BigGAN* [6]. We directly train t on latent codes of the generator model, utilizing a simple variational autoencoder model for dequantization of discrete classes c . See Sec.B.6 for technical details.

Verifying the Texture-Bias Hypothesis In Section 4.3 we trained the INN t conditioned on representations of ResNet-50 from the penultimate layer (*i.e.* extracted before the final classification layer, *c.f.* Tab. S13) with the goal of validating the *texture-bias hypothesis* from [18]. In their work, [18] showed that typical convolutional neural classification networks are biased towards texture when being trained on ImageNet. They proposed that this bias can be removed by training the CNNs on a *stylized* version of ImageNet instead.

Following [49], we gained access to the dataset and a powerful decoder by relying on a synthetic version of ImageNet, provided through the pre-trained generator of BigGAN [6].³ Thus, with Eq. (5) in mind, we identify the concatenated vector $(\tilde{z}, \mathbf{W}c)$ as \tilde{z} . Here, $\mathbb{R}^{140} \ni \tilde{z} \sim \mathcal{N}(0, 1)$ is sampled from a multivariate normal distribution and $c \in \{0, 1\}^K$ is a one-hot vector representing one of the $K = 1000$ ImageNet classes. \mathbf{W} maps the one-hot class representation c to the space of real numbers, *i.e.* $\mathbf{W}c = h \in \mathbb{R}^{128}$. Note that \mathbf{W} is part of the BigGAN generator D_{BIG} and is thus also pre-trained. See Fig. S11 for a visual summary of the application of our approach to BigGAN. To avoid overfitting t on a single dimension of \tilde{z} , the vector h is passed through a small, fully connected variational autoencoder before being concatenated with \tilde{z} as $\tilde{z} = (\tilde{z}, h)$. The architecture of this VAE is depicted in Tab. S17. Utilizing this approach can be interpreted as a variant of deep dequantization. Equipped with a dequantized version of

³ We used a pretrained generator available at <https://github.com/LoreGoetschalckx/GANalyze>

Table S17. Architecture of the VAE used for dequantization when training solely on synthetic BigGAN data. Here, a slope parameter of $\alpha = 0.01$ is used in Leaky ReLU.

Embedding $h \in \mathbb{R}^{128}$
$(\text{FC}, \text{LReLU}) \rightarrow \mathbb{R}^{4096}$
$2 \times (\text{FC}, \text{LReLU}) \rightarrow \mathbb{R}^{4096}$
μ, σ^2 : for each:
$(\text{FC}, \text{LReLU}) \rightarrow \mathbb{R}^{128}$
$(\text{FC}, \text{LReLU}) \rightarrow \mathbb{R}^{4096}$
$2 \times (\text{FC}, \text{LReLU}) \rightarrow \mathbb{R}^{4096}$
$(\text{FC}, \text{LReLU}) \rightarrow \mathbb{R}^{128}$
$h \in \mathbb{R}^{128} \sim \mathcal{N}(\mu, \text{diag}(\sigma^2))$
$(\text{FC}, \text{LReLU}) \rightarrow \mathbb{R}^{4096}$
$3 \times (\text{FC}, \text{LReLU}) \rightarrow \mathbb{R}^{4096}$
$(\text{FC}, \text{LReLU}) \rightarrow \mathbb{R}^{128}$

$\bar{z} = (\tilde{z}, h)$ and corresponding images $x = D_{BIG}(\bar{z})$, we trained t as described in Sec. 3.1.

Additional samples conditioned on representations of (i) a ResNet-50 trained on standard ImageNet and (ii) a ResNet-50 trained on the stylized version of ImageNet are provided in Fig. S12. These results further confirm the texture&shape-bias of (i) and the reverse behavior for (ii). Line 7 and 8 explicitly show that a texture-agnostic classifier can be used to create new content based on input sketches or cartoons.

Furthermore, note that both models perform reasonably well on the domain of natural images, *c.f.* line 1-2 of Tab. S12.

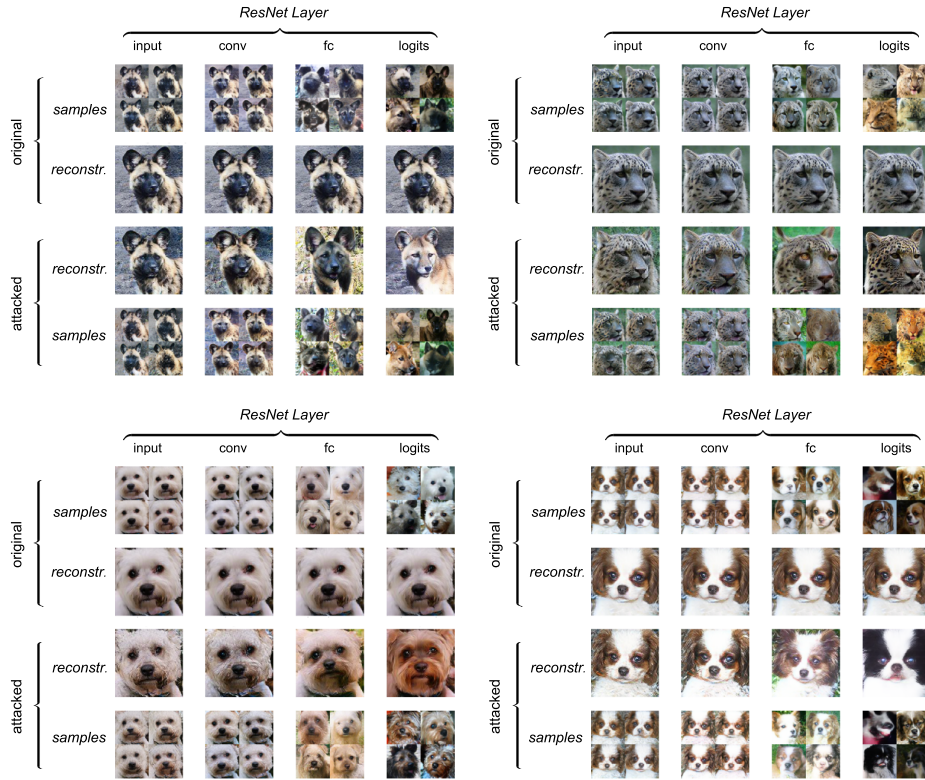


Fig. S13. More visualizations of adversarial attacks as in Fig. 5. Predictions of original *vs.* attacked version of the input image for all depicted examples: *top left:* ‘Lycaon pictus’ *vs.* ‘Cuon alpinus’; *top right:* ‘Snow Leopard’ *vs.* ‘Leopard’; *bottom left:* ‘West Highland white Terrier’ *vs.* ‘Yorkshire Terrier’; *bottom right:* ‘Blenheim Spaniel’ *vs.* ‘Japanese Spaniel’.

References

1. Achille, A., Soatto, S.: Emergence of invariance and disentanglement in deep representations. *The Journal of Machine Learning Research* **19**(1), 1947–1980 (2018)
2. Ardizzone, L., Kruse, J., Wirkert, S., Rahner, D., Pellegrini, E.W., Klessen, R.S., Maier-Hein, L., Rother, C., Köthe, U.: Analyzing inverse problems with invertible neural networks (2018)
3. Bach, S., Binder, A., Montavon, G., Klauschen, F., Müller, K.R., Samek, W.: On pixel-wise explanations for non-linear classifier decisions by layer-wise relevance propagation. *PloS one* **10**(7), e0130140 (2015)
4. Bau, D., Zhou, B., Khosla, A., Oliva, A., Torralba, A.: Network dissection: Quantifying interpretability of deep visual representations. 2017 IEEE Conference on Computer Vision and Pattern Recognition (CVPR) (Jul 2017). <https://doi.org/10.1109/cvpr.2017.354>, <http://dx.doi.org/10.1109/CVPR.2017.354>
5. Bau, D., Zhu, J.Y., Strobel, H., Zhou, B., Tenenbaum, J.B., Freeman, W.T., Torralba, A.: Gan dissection: Visualizing and understanding generative adversarial networks (2018)
6. Brock, A., Donahue, J., Simonyan, K.: Large scale gan training for high fidelity natural image synthesis. arXiv preprint arXiv:1809.11096 (2018)
7. Cao, Q., Shen, L., Xie, W., Parkhi, O.M., Zisserman, A.: Vggface2: A dataset for recognising faces across pose and age. In: 2018 13th IEEE International Conference on Automatic Face & Gesture Recognition (FG 2018). pp. 67–74. IEEE (2018)
8. Choi, Y., Choi, M., Kim, M., Ha, J.W., Kim, S., Choo, J.: Stargan: Unified generative adversarial networks for multi-domain image-to-image translation. In: Proceedings of the IEEE Conference on Computer Vision and Pattern Recognition (2018)
9. Commission, E.: On artificial intelligence - a european approach to excellence and trust. Tech. rep. (2020 (accessed February, 2020)), <https://eur-lex.europa.eu/legal-content/EN/TXT/?uri=COM:2020:65:FIN>
10. Dai, B., Wipf, D.: Diagnosing and enhancing vae models (2019)
11. Deng, J., Dong, W., Socher, R., Li, L.J., Li, K., Fei-Fei, L.: Imagenet: A large-scale hierarchical image database. In: 2009 IEEE conference on computer vision and pattern recognition. pp. 248–255. Ieee (2009)
12. Dinh, L., Sohl-Dickstein, J., Bengio, S.: Density estimation using real nvp (2016)
13. Dosovitskiy, A., Brox, T.: Generating images with perceptual similarity metrics based on deep networks (2016)
14. Esser, P., Haux, J., Ommer, B.: Unsupervised robust disentangling of latent characteristics for image synthesis. 2019 IEEE/CVF International Conference on Computer Vision (ICCV) (Oct 2019). <https://doi.org/10.1109/iccv.2019.00279>, <http://dx.doi.org/10.1109/ICCV.2019.00279>
15. Esser, P., Rombach, R., Ommer, B.: A disentangling invertible interpretation network for explaining latent representations. In: Proceedings of the IEEE/CVF Conference on Computer Vision and Pattern Recognition. pp. 9223–9232 (2020)
16. Fong, R., Vedaldi, A.: Net2vec: Quantifying and explaining how concepts are encoded by filters in deep neural networks. 2018 IEEE/CVF Conference on Computer Vision and Pattern Recognition (Jun 2018). <https://doi.org/10.1109/cvpr.2018.00910>, <http://dx.doi.org/10.1109/CVPR.2018.00910>

17. Fong, R., Vedaldi, A.: Net2vec: Quantifying and explaining how concepts are encoded by filters in deep neural networks. In: Proceedings of the IEEE conference on computer vision and pattern recognition. pp. 8730–8738 (2018)
18. Geirhos, R., Rubisch, P., Michaelis, C., Bethge, M., Wichmann, F.A., Brendel, W.: Imagenet-trained cnns are biased towards texture; increasing shape bias improves accuracy and robustness. arXiv preprint arXiv:1811.12231 (2018)
19. Goetschalckx, L., Andonian, A., Oliva, A., Isola, P.: Ganalyze: Toward visual definitions of cognitive image properties. arXiv preprint arXiv:1906.10112 (2019)
20. Goodfellow, I.J., Shlens, J., Szegedy, C.: Explaining and harnessing adversarial examples. arXiv preprint arXiv:1412.6572 (2014)
21. Goodman, B., Flaxman, S.: European union regulations on algorithmic decision-making and a “right to explanation”. *AI Magazine* **38**(3), 50–57 (Oct 2017). <https://doi.org/10.1609/aimag.v38i3.2741>, <http://dx.doi.org/10.1609/aimag.v38i3.2741>
22. He, K., Zhang, X., Ren, S., Sun, J.: Deep residual learning for image recognition. In: Proceedings of the IEEE conference on computer vision and pattern recognition. pp. 770–778 (2016)
23. Heusel, M., Ramsauer, H., Unterthiner, T., Nessler, B., Hochreiter, S.: Gans trained by a two time-scale update rule converge to a local nash equilibrium (2017)
24. Iandola, F.N., Han, S., Moskewicz, M.W., Ashraf, K., Dally, W.J., Keutzer, K.: Squeezenet: Alexnet-level accuracy with 50x fewer parameters and 0.5 mb model size. arXiv preprint arXiv:1602.07360 (2016)
25. Jacobsen, J.H., Behrmann, J., Zemel, R., Bethge, M.: Excessive invariance causes adversarial vulnerability (2018)
26. Kingma, D.P., Welling, M.: Auto-encoding variational bayes. arXiv preprint arXiv:1312.6114 (2013)
27. Kingma, D.P., Dhariwal, P.: Glow: Generative flow with invertible 1x1 convolutions. In: Advances in Neural Information Processing Systems. pp. 10215–10224 (2018)
28. Kotovenko, D., Sanakoyeu, A., Lang, S., Ommer, B.: Content and style disentanglement for artistic style transfer. 2019 IEEE/CVF International Conference on Computer Vision (ICCV) pp. 4421–4430 (2019)
29. Krizhevsky, A., Sutskever, I., Hinton, G.E.: Imagenet classification with deep convolutional neural networks. In: Advances in neural information processing systems. pp. 1097–1105 (2012)
30. Kulkarni, T.D., Whitney, W., Kohli, P., Tenenbaum, J.B.: Deep convolutional inverse graphics network (2015)
31. LeCun, Y.: The mnist database of handwritten digits. <http://yann.lecun.com/exdb/mnist/> (1998)
32. LeCun, Y.: Learning invariant feature hierarchies. In: European conference on computer vision. pp. 496–505. Springer (2012)
33. Li, Y., Singh, K.K., Ojha, U., Lee, Y.J.: Mixnmatch: Multifactor disentanglement and encoding for conditional image generation (2019)
34. Lipton, Z.C.: The mythos of model interpretability (2016)
35. Liu, M.Y., Huang, X., Mallya, A., Karras, T., Aila, T., Lehtinen, J., Kautz, J.: Few-shot unsupervised image-to-image translation. arXiv preprint arXiv:1905.01723 (2019)
36. Liu, Z., Luo, P., Wang, X., Tang, X.: Deep learning face attributes in the wild. In: Proceedings of International Conference on Computer Vision (ICCV) (December 2015)

37. Locatello, F., Bauer, S., Lucic, M., Rätsch, G., Gelly, S., Schölkopf, B., Bachem, O.: Challenging common assumptions in the unsupervised learning of disentangled representations (2018)
38. Lorenz, D., Bereska, L., Milbich, T., Ommer, B.: Unsupervised part-based disentangling of object shape and appearance. 2019 IEEE/CVF Conference on Computer Vision and Pattern Recognition (CVPR) pp. 10947–10956 (2019)
39. Mahendran, A., Vedaldi, A.: Visualizing deep convolutional neural networks using natural pre-images. *International Journal of Computer Vision* **120**(3), 233–255 (2016)
40. Miller, T.: Explanation in artificial intelligence: Insights from the social sciences. *Artificial Intelligence* **267**, 1–38 (2019)
41. Montavon, G., Lapuschkin, S., Binder, A., Samek, W., Müller, K.R.: Explaining nonlinear classification decisions with deep taylor decomposition. *Pattern Recognition* **65**, 211–222 (2017)
42. Montavon, G., Samek, W., Müller, K.R.: Methods for interpreting and understanding deep neural networks. *Digital Signal Processing* **73**, 1–15 (2018)
43. Mordvintsev, A., Olah, C., Tyka, M.: Inceptionism: Going deeper into neural networks (2015)
44. Nash, C., Kushman, N., Williams, C.K.: Inverting supervised representations with autoregressive neural density models. In: *The 22nd International Conference on Artificial Intelligence and Statistics*. pp. 1620–1629 (2019)
45. Nguyen, A., Dosovitskiy, A., Yosinski, J., Brox, T., Clune, J.: Synthesizing the preferred inputs for neurons in neural networks via deep generator networks (2016)
46. Plumb, G., Al-Shedivat, M., Xing, E., Talwalkar, A.: Regularizing black-box models for improved interpretability (2019)
47. Redlich, A.N.: Supervised factorial learning. *Neural Computation* **5**(5), 750–766 (1993). <https://doi.org/10.1162/neco.1993.5.5.750>
48. Rezende, D.J., Mohamed, S., Wierstra, D.: Stochastic backpropagation and approximate inference in deep generative models. In: *Proceedings of the 31st International Conference on International Conference on Machine Learning-Volume 32*. pp. II–1278. *JMLR. org* (2014)
49. Rombach, R., Esser, P., Ommer, B.: Network fusion for content creation with conditional inns (2020)
50. Samek, W., Wiegand, T., Müller, K.R.: Explainable artificial intelligence: Understanding, visualizing and interpreting deep learning models. arXiv preprint [arXiv:1708.08296](https://arxiv.org/abs/1708.08296) (2017)
51. Santurkar, S., Tsipras, D., Tran, B., Ilyas, A., Engstrom, L., Madry, A.: Image synthesis with a single (robust) classifier (2019)
52. Schroff, F., Kalenichenko, D., Philbin, J.: Facenet: A unified embedding for face recognition and clustering. In: *Proceedings of the IEEE conference on computer vision and pattern recognition*. pp. 815–823 (2015)
53. Selvaraju, R.R., Cogswell, M., Das, A., Vedantam, R., Parikh, D., Batra, D.: Grad-cam: Visual explanations from deep networks via gradient-based localization. *International Journal of Computer Vision* **128**(2), 336–359 (Oct 2019). <https://doi.org/10.1007/s11263-019-01228-7>, <http://dx.doi.org/10.1007/s11263-019-01228-7>
54. Shocher, A., Gandelsman, Y., Mosseri, I., Yarom, M., Irani, M., Freeman, W.T., Dekel, T.: Semantic pyramid for image generation. In: *Proceedings of the IEEE/CVF Conference on Computer Vision and Pattern Recognition (CVPR)* (June 2020)

55. Simon, M., Rodner, E.: Neural activation constellations: Unsupervised part model discovery with convolutional networks. 2015 IEEE International Conference on Computer Vision (ICCV) (Dec 2015). <https://doi.org/10.1109/iccv.2015.136>, <http://dx.doi.org/10.1109/ICCV.2015.136>
56. Simon, M., Rodner, E., Denzler, J.: Part detector discovery in deep convolutional neural networks. ArXiv [abs/1411.3159](https://arxiv.org/abs/1411.3159) (2014)
57. Simonyan, K., Vedaldi, A., Zisserman, A.: Deep inside convolutional networks: Visualising image classification models and saliency maps. arXiv preprint arXiv:1312.6034 (2013)
58. Szegedy, C., Zaremba, W., Sutskever, I., Bruna, J., Erhan, D., Goodfellow, I., Fergus, R.: Intriguing properties of neural networks (2013)
59. Upchurch, P., Gardner, J., Pleiss, G., Pless, R., Snaveley, N., Bala, K., Weinberger, K.: Deep feature interpolation for image content changes. In: Proceedings of the IEEE conference on computer vision and pattern recognition. pp. 7064–7073 (2017)
60. Xian, Y., Lampert, C.H., Schiele, B., Akata, Z.: Zero-shot learning—a comprehensive evaluation of the good, the bad and the ugly. *IEEE transactions on pattern analysis and machine intelligence* **41**(9), 2251–2265 (2018)
61. Xiao, Z., Yan, Q., Amit, Y.: Generative latent flow (2019)
62. Yosinski, J., Clune, J., Nguyen, A., Fuchs, T., Lipson, H.: Understanding neural networks through deep visualization (2015)
63. Zeiler, M.D., Fergus, R.: Visualizing and understanding convolutional networks. *Lecture Notes in Computer Science* p. 818–833 (2014)
64. Zhang, Q., Nian Wu, Y., Zhu, S.C.: Interpretable convolutional neural networks. In: Proceedings of the IEEE Conference on Computer Vision and Pattern Recognition. pp. 8827–8836 (2018)
65. Zhang, R., Isola, P., Efros, A.A., Shechtman, E., Wang, O.: The unreasonable effectiveness of deep features as a perceptual metric. In: CVPR (2018)
66. Zhou, B., Khosla, A., Lapedriza, A., Oliva, A., Torralba, A.: Object detectors emerge in deep scene cnns (2014)
67. Zhou, B., Khosla, A., Lapedriza, A., Oliva, A., Torralba, A.: Learning deep features for discriminative localization. 2016 IEEE Conference on Computer Vision and Pattern Recognition (CVPR) (Jun 2016). <https://doi.org/10.1109/cvpr.2016.319>, <http://dx.doi.org/10.1109/CVPR.2016.319>